Large-eddy simulations of turbulent heat transfer in stationary and rotating square ducts

Jordi Pallares
Department of Mechanical Engineering, Universitat Rovira i Virgili, 43007 Tarragona, Spain

Lars Davidson
Department of Thermo and Fluid Dynamics, Chalmers University of Technology, 41296 Gothenburg, Sweden

(Received 28 June 2001; accepted 8 May 2002; published 2 July 2002)

Turbulent heat transfer at low Reynolds numbers in stationary and rotating straight square ducts was simulated using the large-eddy simulation technique. For the rotating square duct flows, the rotation axis was parallel to two opposite walls of the duct. The pressure-driven flow was assumed to be hydrodynamically and thermally fully developed. A constant and uniform heat flux distribution in the axial direction was applied at the four smooth walls of the forced and mixed convection flows. Two boundary conditions for the thermal energy equation were examined: constant peripheral wall temperature and uniform peripheral wall heat flux. Computations were carried out using a second-order finite volume code with a localized one-equation dynamic subgrid scale model. For the simulated nonrotating flows, there were significant differences of about 16% in the overall Nusselt numbers, depending on the type of thermal boundary condition applied at the walls. This was because of the presence of the corners. Simulations of mixed convection arising from the centrifugal buoyancy effect showed that the turbulence level of the flow was strongly influenced by the centrifugal buoyancy effect. At the rotation rate considered, the overall Nusselt numbers and the turbulence levels of the flow were not greatly affected by the type of boundary conditions for temperature applied at the walls. However, temperature fluctuation intensities noticeably increased when a uniform peripheral heat flux was imposed at the walls. © *2002 American Institute of Physics.* [DOI: 10.1063/1.1489684]

I. INTRODUCTION

Heat transfer rates in straight ducts subjected to rotation around an axis perpendicular to the streamwise flow direction are influenced by the induced Coriolis and centrifugal buoyancy forces. Rotating channel studies have shown that the Coriolis force affects the turbulence level of the flow.[1–3] Turbulent mixing of fluid particles is enhanced in the regions of the flow where the stratification of the streamwise momentum is unstable with respect to the Coriolis force (pressure side), whereas mixing is reduced where the stratification of the streamwise momentum is stable (suction side). In finite aspect ratio ducts, the Coriolis force generates persistent secondary flows, which contribute to the mixing processes between the stable and unstable sides of the duct.[4,5] At high rotation rates, density gradients within the flow may produce different centrifugal accelerations in regions of the flow with different local temperatures.[6,7] This complex physical situation, where the rotation effects are linked through the coupled nonlinear momentum and thermal energy differential balances, has important implications in technological fields such as internal blade cooling, where flow and heat transfer take place in rotating devices.

Heat transfer processes in wall-bounded flows are influenced by the heating or cooling mechanisms at the walls. Numerical simulations usually model the peripheral heat transfer flux by imposing uniform constant temperature[6,8–10] or a uniform heat flux[4,11] along the whole surface of the walls. A uniform heat flux axial distribution and constant wall temperature at a given axial position has been used in numerical studies dealing with heat transfer in nonrotating fully developed channel flow.[11] This boundary condition sets temperature fluctuations on the walls to zero by assuming high heat conduction along the duct periphery. However, certain conditions, such as low thermal conductance of the walls, the presence of sharp corners, and the coexistence of regions of the flow with different turbulence levels can produce significant variation in the wall temperatures along the duct periphery. In these situations, the wall temperature distributions can be modeled by the uniform heat flux boundary condition, which has been used to study the wall temperature fluctuations produced by the near-wall turbulent structures in channel flows.[12,13] Information obtained from the temperature fluctuation intensities at the walls can be used to predict thermal fatigue in the solid boundary structure.

This study analyzes turbulent forced and mixed convection arising from the centrifugal buoyancy force in stationary and rotating square ducts at low Reynolds numbers. The effects of two different thermal boundary conditions that allow different levels of temperature fluctuations at the walls are examined. A second-order finite volume code with a localized dynamic one-equation subgrid scale model[14] has been used to numerically solve the governing transport equations for several combinations of system parameters (rotational

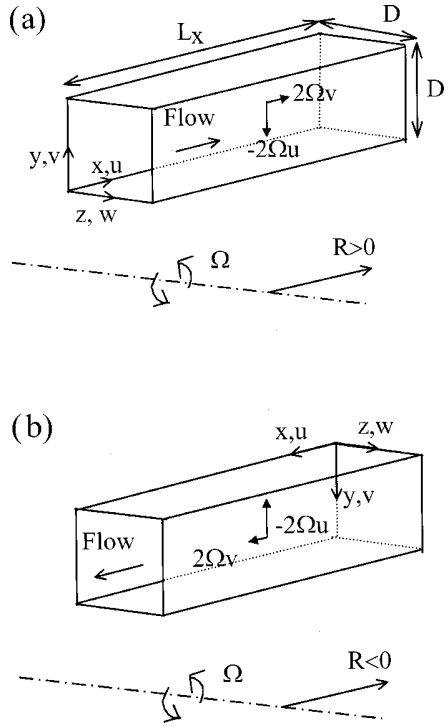

FIG. 1. Physical model and coordinate system. (a) Outward flow, (b) inward flow.

and Grashof numbers and thermal boundary conditions). The physical and mathematical models are described in Sec. II and the results are presented and discussed in Sec. III.

II. MODEL

Figure 1 shows the physical model of the straight duct and the coordinate system adopted. The entire system rotates with a constant positive angular velocity, Ω, parallel to the z direction. Figure 1 also shows the components of the Coriolis acceleration. The radius of rotation, $R=\sqrt{X_r^2+Y_r^2}$, is assumed to be constant, which is the case in the coolant passages of a turbine blade whose height is smaller than the radius of the turbine rotor disc. The externally imposed pressure gradient between the inlet and the outlet of the duct can drive the flow radially inwards [Fig. 1(a)] or radially outwards [Fig. 1(b)]. The four walls are smooth and they are heated with a constant and uniformly distributed heat flux along the axial direction. The physical properties of the fluid with a Prandtl number of 0.71 are assumed to be constant with temperature. Only a linear dependence of the temperature on density is taken into account to model the centrifugal buoyancy effect according to the Boussinesq approximation.

The gravitational inertia is neglected in comparison with the rotational induced centrifugal effect. Two different thermal boundary conditions at the duct walls have been investigated and are denoted as H1 and H2 following the nomenclature of Shah and Bhatti.[15] The H1 boundary condition assumes a constant axial wall heat flux with constant peripheral wall temperature, while the H2 boundary condition assumes a constant axial wall heat flux with uniform peripheral wall heat flux. The H1 and H2 boundary conditions idealize practical situations in which the axial heat rate per duct length is constant and the wall conductance (C), defined in Eq. (1), has high and low values, respectively.

$$C=k^*d^*=\frac{k_w}{k}\frac{D}{d}. \tag{1}$$

In Eq. (1), k^* is the ratio between the wall (k_w) and the fluid (k) thermal conductivities and d^* is the ratio between the hydraulic diameter of the duct (D) and the wall thickness (d).

The large-eddy simulation (LES) technique has been chosen to keep the computational requirements at a moderate level. LES is based on decomposition of the flow variables into a large-scale (or resolved) component and a subgrid scale component. The resolved scales and the corresponding governing transport equations are defined by the filtering operation. The nondimensional filtered continuity, Navier–Stokes and energy transport equations are

$$\frac{\partial u_i}{\partial x_i}=0, \tag{2}$$

$$\frac{\partial u_i}{\partial t}+\frac{\partial u_j u_i}{\partial x_j}=4\,\delta_{1i}-\frac{\partial p}{\partial x_i}-\frac{\partial \tau_{ij}}{\partial x_j}+\frac{1}{\mathrm{Re}_\tau}\frac{\partial^2 u_i}{\partial x_j \partial x_j}+\in_{ij3}\mathrm{Ro}_\tau u_j-\frac{\mathrm{Gr}_\tau}{\mathrm{Re}_\tau^2}\left(\theta+\frac{(4x-2L_x)}{U_b}\right)\delta_{1i}, \tag{3a}$$

and

$$\frac{\partial \theta}{\partial t}+\frac{\partial u_j \theta}{\partial x_j}=-4\,\delta_{1j}\frac{u_j}{U_b}-\frac{\partial h_j}{\partial x_j}+\frac{1}{\mathrm{Pr}\,\mathrm{Re}_\tau}\frac{\partial^2 \theta}{\partial x_j \partial x_j}, \tag{4}$$

respectively. The scales used to obtain the nondimensional variables are the hydraulic diameter (D) and the average friction velocity (u_τ) based on the pressure gradient, see Eq. (5). Temperature and pressure have been scaled with the friction temperature ($T_\tau=q_w''/\rho C_p u_\tau$) and ρu_τ^2, respectively. According to the definition of θ used here, $\theta=(T-\langle T\rangle_w)/T_\tau$, positive/negative values of θ correspond to higher/lower local temperatures with respect to the peripherally averaged wall temperature $\langle T\rangle_w$, at a given axial position. The nondimensional parameters in Eqs. (2)–(4) are the Reynolds number ($\mathrm{Re}_\tau=u_\tau D/\nu$), the rotational number ($\mathrm{Ro}_\tau=2\Omega D/u_\tau$), the Prandtl number ($\mathrm{Pr}=\nu/\alpha=\mu C_p/k$), and the Grashof number ($\mathrm{Gr}_\tau=R\Omega^2\beta T_\tau D^3/\nu^2$).

The first term on the right-hand side of Eq. (3a) corresponds to the nondimensional imposed constant pressure gradient along the x direction. In Eqs. (3a) and (4), the terms $\partial\tau_{ij}/\Omega x_j$ and $\partial h_j/\partial x_j$, which are the SGS contributions to the momentum and energy transfers, arise from the filtering of the Navier–Stokes and thermal energy equations. The fifth and sixth terms on the right-hand side of Eq. (3a) are the Coriolis and the centrifugal buoyancy terms, respectively. It can be seen that the centrifugal buoyancy term has only been considered in the x-momentum equation by assuming $X_r \gg Y_r$. The first term on the right-hand side of Eq. (4) corresponds to $ud\langle T\rangle_w/dx$, according to the assumption that the flow and thermal fields are fully developed (i.e., the wall temperature ensemble averaged over the x direction increases

linearly along the x direction and therefore, $d\langle T\rangle_w/dx = dT_b/dx = 4q''_w/\rho C_p U_b$, where T_b and U_b are the dimensional bulk temperature and the bulk velocity, respectively).

The nondimensionalization of the temperature field and the decomposition of the pressure field into a constant mean value and a fluctuating term have been chosen to apply periodic boundary conditions for u_i, p, and θ at $x=0$ and $x=L_x$. Pallares and Davidson[5] reported that time and x-direction averaging should be carried out for about 50 letots (10 000 time steps) in an isothermal fully developed rotating square duct flow to obtain representative averaged flow fields.

It can be seen that the second part of the last term in Eq. (3a), which corresponds to the rotational centrifugal buoyancy effect in the x-momentum equation, is not periodic because it contains the streamwise coordinate. However, for the flow conditions simulated in this study the maximum value of the term, $-\mathrm{Gr}_\tau/\mathrm{Re}_\tau^2((4x-2L_x)/U_b)$, is 2.5% of the mean imposed pressure gradient, which is the driving force of the flow in the x direction. This shows that the flow, in the range of nondimensional parameters studied, can be considered as a good approximation hydrodynamically and thermally fully developed in the computational domain used. Consequently, this term has been neglected and Eq. (3a) can be rewritten as

$$\frac{\partial u_i}{\partial t}+\frac{\partial u_j u_i}{\partial x_j}=4\delta_{1i}-\frac{\partial p}{\partial x_i}-\frac{\partial \tau_{ij}}{\partial x_j}+\frac{1}{\mathrm{Re}_\tau}\frac{\partial^2 u_i}{\partial x_j \partial x_j} + \in_{ij3}\mathrm{Ro}_\tau u_j-\frac{\mathrm{Gr}_\tau}{\mathrm{Re}_\tau^2}\theta\delta_{1i}. \tag{3b}$$

The governing transport equations [Eqs. (2), (3b), and (4)] and boundary conditions have been solved numerically with the CALC–LES code,[16,17] a second-order accuracy finite volume code that uses central differencing of the diffusive and convective terms on a collocated grid and a Crank–Nicolson scheme for the temporal discretization. The coupling between the velocity and pressure fields was solved efficiently by an implicit, two-step, time advancement method and a multigrid solver[18] for the resulting Poisson equation.

In this study, the subgrid scale stresses have been computed following the localized one-equation dynamic SGS model proposed by Kim and Menon.[14] The complete formulation of the SGS model can be found elsewhere.[5,19] As in other SGS models, the anisotropic part of the SGS stress tensor is assumed to be aligned with the resolved local strain rate tensor ($\tau_{ij}-\delta_{ij}\tau_{kk}/3=-2\nu_{\mathrm{SGS}}S_{ij}$) and the SGS heat fluxes (h_j) are modeled in analogy to τ_{ij} ($h_j=-\alpha_{\mathrm{SGS}}\partial\theta/\partial x_j$). The model used enables the calculated SGS viscosity (ν_{SGS}) to vary in space and time without any spatial averaging of the model coefficients. It is important to note that a localized SGS model is essential in the simulations of the rotating duct or channel flows because of the stabilizing/destabilizing effect of rotation on turbulence in different regions of the flow.

According to *a priori* tests,[8] the SGS Prandt number ($\mathrm{Pr}_{\mathrm{SGS}}=\nu_{\mathrm{SGS}}/\alpha_{\mathrm{SGS}}$) for air ($\mathrm{Pr}=0.7$) in forced convection channel flow ranges from $\mathrm{Pr}_{\mathrm{SGS}}\approx 0.4$ in the central part of the channel to $\mathrm{Pr}_{\mathrm{SGS}}\approx 1$ near the wall. Turbulent forced convection channel flow using constant SGS Prandtl number ($\mathrm{Pr}_{\mathrm{SGS}}=0.4$) was initially carried out[19] and profiles of the mean temperature and turbulence heat fluxes were in very good agreement with DNS of Kasagi *et al.*[11] On the other hand, the comparison of two simulations of forced convection in a rotating duct at $\mathrm{Ro}_\tau=1.5$ using $\mathrm{Pr}_{\mathrm{SGS}}=0.4$ and $\mathrm{Pr}_{\mathrm{SGS}}=0.8$ showed no significant differences in the primary statistics of the flow. For these reasons $\mathrm{Pr}_{\mathrm{SGS}}=0.4$ has been used in all the simulations.

The computational domain, with dimensions $L_x\approx 6D$, $L_y=D$, $L_z=D$, was divided into $66\times66\times66$ grid nodes. These were uniformly distributed along the x direction, $\Delta x^+\approx 29$, in which periodic boundary conditions were imposed for velocity, pressures, and temperature, while tanh distributions were used to stretch the nodes near the walls where no-slip condition for velocity was applied. For the Reynolds number considered, the minimum and maximum grid spacing in wall coordinates in the directions perpendicular to the walls are $(\Delta y^+)_{\min}=(\Delta z^+)_{\min}\approx 0.4$ and $(\Delta y^+)_{\max}=(\Delta z^+)_{\max}\approx 9$. A constant wall temperature, $\theta_w=0$ (i.e., $\theta'_w=0$) was imposed at the four walls when the H1 boundary conditions was simulated, while a constant value of the nondimensional temperature gradient perpendicular to the wall was used for the thermal boundary condition H2 ($\partial\theta/\partial n)_w=-\mathrm{Re}_\tau\mathrm{Pr}$ (i.e., $\theta'_w\neq 0$).

Large-eddy simulations of the non-rotating channel ($\mathrm{Re}_\tau=194$, $\mathrm{Re}\approx 6200$) and duct flows ($\mathrm{Re}_\tau=300$, $\mathrm{Re}\approx 4500$), and rotating channel flows ($\mathrm{Re}_\tau=194$, $\mathrm{Ro}_\tau=1.5$, and $\mathrm{Ro}_\tau=3.6$) using the CALC–LES code with the grid resolution used in this study compare favorably with DNS and experimental data in previous studies.[5,19] Pallares and Davidson[19] showed that the increase in the turbulent activity generated by rotation in channel flows up to $\mathrm{Ro}_\tau=3.6$ is adequately reproduced by the grid spacing used in this study.

Simulations of forced convection were started from isothermal fully developed instantaneous flow fields at $\mathrm{Re}_\tau=300$. The sampling procedure for obtaining the average velocity and temperature fields and the turbulent intensities was not started until the flow was statistically fully developed. The flow quantities were averaged along the homogeneous x direction and in time over about 50–70 nondimensional time units representing about 140–180 h of CPU time using one CPU of an Origin 2000 SGI computer. Mixed convection results were obtained using instantaneous fully developed forced convection fields as initial conditions. Simulations were conducted until a new statistically steady state was reached. The macroscopic momentum and energy balances for the averaged flow and thermal fields were within 0.1% in all the simulations in this study.

III. RESULTS AND DISCUSSION

A. Mean flow and temperature fields

Table I shows the set of simulations carried out in this study, in which the Reynolds number based on the friction velocity was kept constant ($\mathrm{Re}_\tau=300$) (i.e., constant imposed pressure gradient). Turbulent forced convection in a nonrotating square duct flow has been computed as the reference case and to determine the effect of the H1 and H2

TABLE I. Mean flow quantities for the different flow conditions simulated at $\mathrm{Re}_\tau=300$ and $\mathrm{Pr}=0.71$.

Ro_τ	Gr_τ	BC	$\langle u^* \rangle_w$	U_b	Θ_b	Ro	Re	Nu	$100\ K/U_b^2$
0	0	H1	1.000	15.1	−14.6	0	4500	14.56	0.94
		H2			−16.9			12.57	
		H1		13.0	−12.6	0.12	3900	16.84	0.51
		H2			−12.6			16.89	
1.5	9000	H1	1.127	16.0	−12.0	0.09	4800	17.72	0.95
	−9000		0.842	10.1	−13.7	0.15	3000	15.51	0.39
	9000	H2	1.123	15.8	−12.0	0.09	4700	17.78	0.97
	−9000		0.849	10.2	−13.5	0.15	3100	15.79	0.38

boundary conditions, which to our knowledge has not been previously reported. Three different Grashof numbers, $\mathrm{Gr}_\tau=0$, $\mathrm{Gr}_\tau=+9000$, and $\mathrm{Gr}_\tau=-9000$ have been used in the simulations of the rotating flows, in which the rotation number ($\mathrm{Ro}_\tau=1.5$) was kept constant to analyze the influence of the centrifugal buoyancy effect. All the rotating cases were calculated with the H1 and H2 thermal boundary conditions. The nondimensional averaged friction velocities (u_τ), bulk velocities (U_b) and bulk temperatures (Θ_b) for the whole set of simulations are shown in Table I. The nondimensional parameters based on the bulk velocity and the hydraulic diameter ($\mathrm{Re}=\mathrm{Re}_\tau U_b$, $\mathrm{Ro}=\mathrm{Ro}_\tau/U_b$) have been also included in Table I. The averaged turbulent kinetic energy (K) in Table I has been scaled with the bulk velocity to make the values at different Reynolds numbers more comparable.

The set of nondimensional parameters ($\mathrm{Re}_\tau=300$, $\mathrm{Ro}_\tau=1.5$, $\mathrm{Pr}=0.71$, and $\mathrm{Gr}_\tau=9000$, 0, −9000) has been chosen because it is possible to carry out experiments[20] in long small ducts ($R=1.5$ m, $D=0.01$ m) at moderate rotation speeds ($\Omega=36$ rad/s) using air flows ($U_b=7.5$ m/s) at ambient temperature ($T_0=293$ K) and pressure. In these conditions, small wall heat fluxes ($q''_w\approx 200$ W/m^2, i.e., $\mathrm{Gr}_\tau\approx 9000$) produce wall temperatures that are about 5 °C higher than the bulk temperature of the fluid. This difference in temperature induces maximum variations in density, thermal conductivity and dynamic viscosity of 1.5%, 0.8%, 0.6%, respectively. This shows that for these physical situations, using the Boussinesq approximation is justified.

Figure 2 shows the resolved averaged thermal and flow fields for the flow conditions simulated in this study. Contours of the streamwise velocity component and the cross stream vector field are shown in the right half of the duct in Figs. 2(a)–2(d), while temperature contours are shown in the left half. The distributions of the local heat fluxes for the H1 flows and wall temperatures for the H2 flows on the periphery of the duct are shown in Figs. 3(a) and 3(b), respectively.

1. Forced convection in a nonrotating duct

Averaged thermal and velocity fields of turbulent forced convection flows in a nonrotating square duct are symmetrical to the wall and corner bisectors.[21,22] Time and x-averaged fields have been averaged in the eight octants of the cross section of the duct. The maximum difference between octant averaged fields and time and x-averaged fields was about 3% for U and Θ. Figure 2(a) shows that the mean cross-stream flow consists of eight counter-rotating vortices, which are distributed in pairs in the four quadrants of the duct. These secondary flows convect cold high momentum fluid from the central region of the duct to the corner region along the corner bisectors as can be deduced from the distortion of the contours of temperature and axial velocity component, shown in Figs. 2(a1)–2(a3). Present predictions of the bulk velocity ($U_b=15.1u_\tau$) and averaged turbulent kinetic energy ($K=2.1u_\tau^2$) agree well with the DNS values from Gavrilakis[21] at the same value of Re_τ ($U_b=14.7u_\tau$ and $K=2.1u_\tau^2$).

Comparison of Figs. 2(a1) (H1 flow) and 2(a2) (H2 flow) shows that, away from the wall, the H2 thermal field has lower temperatures and higher temperature gradients than the H1 thermal field. This is especially so near the corners, where the averaged temperature of the H2 flow is higher than the peripherally averaged wall temperature (i.e., $\Theta>0$). It can be seen, for example, that the distance between the contours $\Theta=-10$ and $\Theta=-15$ is almost twice as long in Fig. 2(a1) as it is in Fig. 2(a2). It should be noted that the imposed average heat flux around the periphery of the duct is in the same in both thermal fields. Consequently, the simulated H1 and H2 flows have the same values of $d\langle T\rangle_w/dx$ and dT_b/dx. Near the corners, where the flow is almost stagnant, the H2 boundary condition produces a higher local wall heat flux than the H1 flow. Accordingly, the nondimensional bulk temperature (Θ_b) and the Nusselt number ($\mathrm{Nu}=h\,D/k=-\mathrm{Re}_\tau\mathrm{Pr}/\Theta_b$) for the H2 flow are as in laminar forced convection in a square duct[15] about 16% lower than for the H1 flow (see Table I). The Nusselt number for the H1 flow ($\mathrm{Nu}=14.56$) is as predicted by Gnielisky's correlation.[23]

Figures 3(a) and 3(b) show that at $\mathrm{Ro}_\tau=0$ low wall heat transfer rates for the H1 flow [Fig. 3(a)] and high wall temperatures for the H2 flow [Fig. 3(b)] occur near the corners according to the reduced main strains ($\partial U/\partial y$ and $\partial U/\partial z$) and, therefore, the streamwise convection heat transfer in these regions. Local heat transfer distribution at the bottom wall [Fig. 3(a)] for the H1 flow has two symmetrically distributed absolute maxima at about 0.18 D from the sidewalls. The positions of these maxima agree with the positions of the local maximum friction velocities (u_τ), according to the conventional analogy of the momentum and heat transfer in the viscous sublayer. This analogy can be written, using the present adimensionalization, as $\mathrm{Pr}\,\partial U/\partial y\approx-\partial\Theta/\partial y$. The H2 boundary condition imposes a constant heat flux along the wall. Figure 3(b) shows the corresponding wall temperature distributions at $\mathrm{Ro}_\tau=0$. Note that in these conditions,

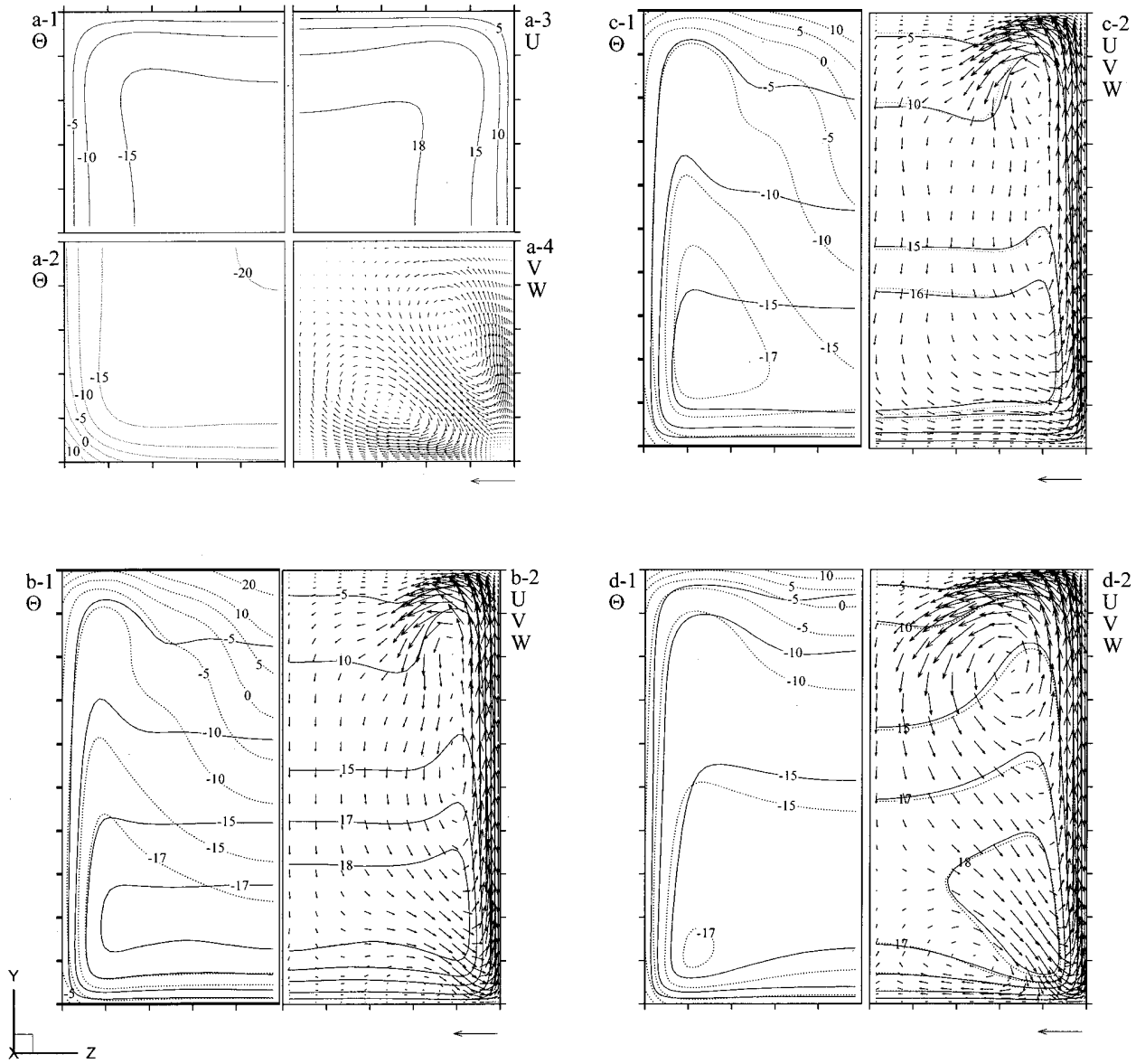

FIG. 2. Resolved averaged mean flow and thermal fields at $Re_\tau = 300$ and $Pr = 0.71$ in terms of axial velocity component and temperature contours and cross-stream vector fields. Continuous-line contours correspond to flow and thermal fields obtained with the H1 boundary condition and dotted line contours correspond to flow and thermal fields with the H2 boundary condition. (a) Forced convection in a nonrotating duct, (b) forced convection in a rotating duct at $Ro_\tau = 1.5$, (c) mixed convection in a rotating duct at $Ro_\tau = 1.5$ and $Gr_\tau = -9000$, and (d) mixed convection in a rotating duct at $Ro_\tau = 1.5$ and $Gr_\tau = +9000$. The vectors located near the bottom right of the graphs have a unit length. In Figs. 1(b)—1(d) only half of the vectors in each direction are shown.

the analogy between momentum and heat transfer in the viscous sublayer does not hold, because the boundary conditions for the momentum and energy equations are different. It can be inferred from Fig. 3(b) that the heat conduction along the wall between the hot corners and the cold wall bisectors tends, for the present nonrotating flow conditions, to inhibit the presence of local temperature minima at the wall away from the wall bisector.

2. Forced convection in a rotating duct

Time and x-direction averaged fields in a rotating duct at $Re_\tau = 300$ tend to be symmetric with respect to the horizontal wall bisector ($z = 0.5$) as the sampling size is increased.[5] Consequently, time and x-direction averaged fields have been further averaged with respect to $z = 0.5$. Maximum differences between the time and x-averaged fields in the two halves of the cross section are about 3% for U and Θ.

At the rotation rate considered in this study ($Ro_\tau = 1.5$), the cross-stream velocity field of a forced convection flow [Fig. 2(b2)], consists of two large and two small counter-rotating cells. The large cells, generated by the vertical component of the Coriolis force (see Fig. 1), convect hot low momentum fluid from the stable side to the unstable side across the central part of the duct. Correspondingly, there were ascending currents near the side walls where the streamwise velocity component and, therefore, the vertical Coriolis force were reduced by the presence of the walls. This convective transport displaces maxima of the axial ve-

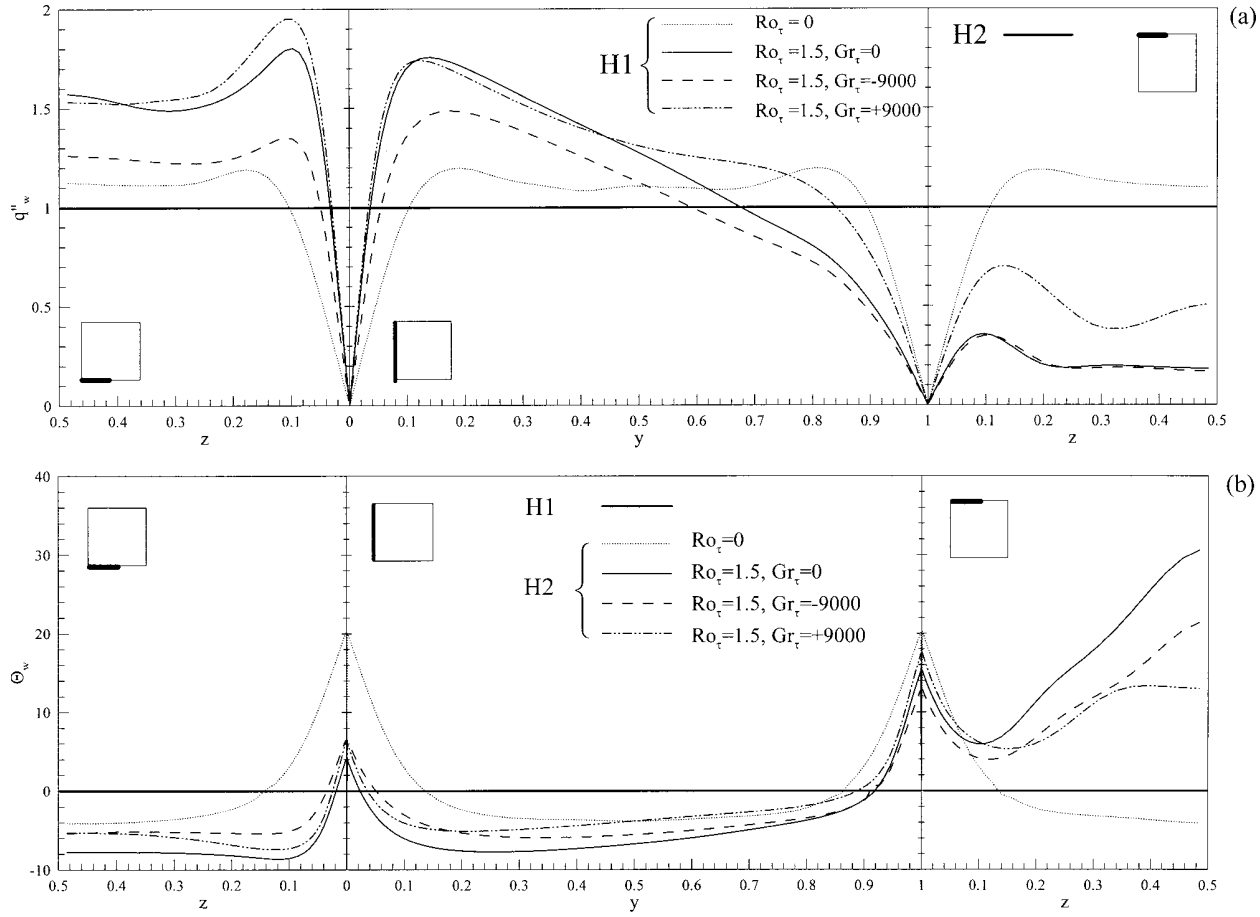

FIG. 3. Distributions of local wall heat fluxes (a) and wall temperatures (b) along the duct periphery. Note that for the case H1, $\theta_w \equiv 0$ and for the case H2 $q''_w \equiv 0$.

locity component and minima of temperature towards the bottom corners [see Figs. 2(b1) and 2(b2)]. At the Reynolds and rotational numbers considered, the level of turbulence on the stable side was considerably reduced owing to the stabilization of the flow in the central part of the duct to a Taylor–Proudman regime, which is characterized by the absence of streamwise vorticity. As Fig. 2(b1) shows, temperatures were higher on the stable side where the effect of the rotation was stabilizing (i.e., turbulence intensities and main shear stresses were lower than in the nonrotating cases[5]). On the unstable side, where rotation imposes unstable x-momentum stratification, stretched small turbulence-driven secondary flows occurred below the corner bisectors and the turbulence level of the flow was higher than in the nonrotating case.[5] This considerably decreased the temperature of the fluid in this region [see Fig. 2(b1)]. As shown in Table I, the overall effect of rotation was stabilizing. It produced a reduction, compared with the nonrotating case, of the overall turbulence level of the flow by about 44%. Figure 2(b1) shows that the isotherms corresponding to the H1 boundary condition (continuous lines) were, like the U contours [Fig. 2(b2)], stratified in the central part of the duct, which indicates the absence of heat transfer along the z direction. On the other hand, the H2 thermal field in Fig. 2(b1) (dotted lines) had important temperature gradients in the z direction, as previously reported by Murata and Mochizuki[4] at higher Reynolds numbers. Table I shows that, for the present rotating flow conditions, the H1 and H2 flows produce similar Nusselt numbers which are about 16% (H1) and 35% (H2) higher than the corresponding nonrotating cases despite the reduction of the Reynolds number. This increase of the Nusselt numbers can be attributed, considering the reduction of the overall turbulence level of the flow, to the augmentation of the role of secondary cells in convecting thermal energy from the hot stable side to the cold unstable side.

As can be inferred from Figs. 3(a) and 3(b), rotation enhances heat transfer mechanisms on the unstable ($y=0$) and lateral walls and decreases heat transfer rates on the stable wall ($y=1$), according to the changes that the cross-stream convection, generated by rotation, produces in the x momentum field. It can be seen in Fig. 3(a) that the position of maximum local heat transfer for the H1 flow on the horizontal walls, as well as that of local u_τ (not shown), shifted towards the corners as the rotation number Ro_τ increased from 0 to 15. Comparison of Figs. 2(a3) to 2(b2) shows that convection of high x-momentum fluid by the secondary velocities towards the bottom corners increased the local main shear stress ($\partial U/\partial y$) in these regions. Local wall heat fluxes near the bottom/top corners increased/decreased at $\mathrm{Ro}_\tau = 1.5$ according to how rotation affected the averaged veloc-

ity fields [see Figs. 2(a3) and 2(b2)]. The wall temperature distribution at $\mathrm{Ro}_\tau = 1.5$ for the H2 flow [Fig. 3(b)] shows that corner temperatures were lower than for the nonrotating H2 flow. Local minimum wall temperatures on the horizontal walls were at 0.1 D, which corresponds to the location of the maximum local friction velocity and the stagnation point generated by large and small cells [see Fig. 2(b2)].

3. Mixed convection in a rotating duct

Figures 2(c) and 2(d) show the averaged thermal and velocity fields of the mixed convection flows at $\mathrm{Gr}_\tau = -9000$ and $\mathrm{Gr}_\tau = 9000$, respectively. Averaged fields of the H1 flows are represented by continuous lines, while averaged thermal and velocity distributions of H2 flows are represented with dotted lines. the cross-stream vector fields in Figs. 2(c2) and 2(d2) correspond to the H1 boundary condition. Secondary flow vector fields at the H2 flows are very similar to those in Figs. 2(c2) and 2(d2) and have been omitted.

Centrifugal buoyancy in the x-momentum equation, $-\mathrm{Gr}_\tau \theta/\mathrm{Re}_\tau^2$ [see Eq. (3b)], can adopt positive or negative values depending on the sign of the Grashof number and θ. The sign of the Grashof number is determined by the direction of the flow with respect to the axis of rotation (see Fig. 1). Centrifugal buoyancy tends to accelerate flows when $\mathrm{Gr}_\tau > 0$ and $\theta < 0$ or when $\mathrm{Gr}_\tau < 0$ and $\theta > 0$, i.e., buoyancy-assisted flow. Correspondingly, it decelerates flow in regions where $\theta > 0$ when $\mathrm{Gr}_\tau > 0$ and where $\theta < 0$ when $\mathrm{Gr}_\tau < 0$, i.e., buoyancy-opposed flow.

When centrifugal buoyancy is considered the mean x-momentum macroscopic balance can be written in nondimensional form as

$$1 = \langle u^* \rangle_w^2 - \frac{\mathrm{Gr}_\tau \langle \Theta \rangle_V}{4\mathrm{Re}_\tau^2}, \tag{5}$$

where $\langle u^* \rangle_w$ is the average friction velocity corresponding to the wall shear stress at the four walls and $\langle \Theta \rangle_V$ is the time and volume-averaged temperature. Equation (5) shows that when buoyancy is taken into account, the mean pressure gradient between the inlet and the outlet of the duct is balanced by the mean wall shear stress and by the centrifugal buoyancy body force. Note that in the present simulations the velocity scale is the friction velocity corresponding to mean pressure gradient (u_τ), which has been kept constant in all cases. Velocity and temperature fields in Figs. 2(c), 2(d), and 3(b) have been scaled with the averaged wall shear stress friction velocities, $\langle u^* \rangle_w$, shown in Table I to make the results at $\mathrm{Gr}_\tau \neq 0$ easier to compare with those at $\mathrm{Gr}_\tau = 0$.

It can be seen comparing Fig. 2(b2) ($\mathrm{Gr}_\tau = 0$) and Figs. 2(c2) ($\mathrm{Gr}_\tau = -9000$) and 2(d2) ($\mathrm{Gr}_\tau = +9000$) that the flow was considerably affected by centrifugal buoyancy. Figure 2(c) shows that both the x-momentum and thermal energy level of the rotation-stabilized flow were lower at $\mathrm{Gr}_\tau = -9000$. The small turbulence-driven cells below the bottom corner bisectors at $\mathrm{Gr}_\tau = 0$, shown in Fig. 2(b), are suppressed at $\mathrm{Gr}_\tau = -9000$ [Fig. 2(c2)]. Figure 2(d2) shows that at $\mathrm{Gr}_\tau = 9000$ the Taylor–Proudman regime in the central part of the duct was suppressed and both secondary cells were enlarged. Maximum streamwise velocities were displaced towards the bottom corner bisectors by the changes in the topology of the secondary cells. Velocity contours in Figs. 2(c2) and 2(d2) were not strongly influenced by the type of thermal boundary condition applied at the walls. As Table I shows, the bulk velocity and the bulk temperature were about the same for the H1 and H2 flows at $\mathrm{Gr}_\tau = -9000$ and $\mathrm{Gr}_\tau = +9000$.

Table I shows that at $\mathrm{Gr}_\tau = +9000$ the overall turbulence level and the Nusselt numbers of the nixed convection flows were about 88% and 5% higher, respectively, than those of the rotating forced convection flow. Correspondingly, the overall turbulence level of the flow and the Nusselt numbers were 25% and 7% lower at $\mathrm{Gr}_\tau = -9000$ than those of the rotating flow at $\mathrm{Gr}_\tau = 0$. The size of these changes is partly due to the lower rotational number, Ro (see Table I). To determine the effect of the change in the bulk velocity and therefore in the Reynolds and rotational numbers when Gr_τ is modified, simulations of H1 mixed convection flows, keeping the bulk velocity constant and adjusting the driving pressure gradient (i.e., $\mathrm{Re} = 3900$ and $\mathrm{Ro} = 0.12$) were conducted. The Grashof numbers based on the wall heat flux ($\mathrm{Gr} = X_r \Omega^2 \beta q_w'' D^4 / k \nu^2 = \mathrm{Gr}_\tau \mathrm{Pr} \mathrm{Re}_\tau$) were 1.9×10^6 for the buoyancy assisted flow and -1.9×10^6 for the buoyancy-opposed flow at $\mathrm{Re} = 3900$ and $\mathrm{Ro} = 0.12$. The topology of the averaged thermal and velocity fields of these simulations agreed with those of simulations obtained with constant pressure gradient shown in Figs. 2(c) and 2(d). The values of the averaged turbulent kinetic energy at $\mathrm{Re} = 3900$ and $\mathrm{Ro} = 0.12$ for $\mathrm{Gr} = 1.9 \times 10^6$ and $\mathrm{Gr} = -1.9 \times 10^6$ were 0.92 and 0.40, respectively. These agree with the values in Table I at $\mathrm{Re} = 4800$ ($100\ \mathrm{K}/U_b^2 = 0.95$) and $\mathrm{Re} = 3000$ ($100\ \mathrm{K}/U_b^2 = 0.39$). The averaged Nusselt numbers of the simulations at $\mathrm{Re} = 3900$ and $\mathrm{Ro} = 0.12$ were 16.7 at $\mathrm{Gr} = 1.9 \times 10^6$ and 16.9 at $\mathrm{Gr} = -1.9 \times 10^6$. These values differ less than 1% in comparison with the Nusselt number of the H1 flow at $\mathrm{Gr} = 0$ ($\mathrm{Nu} = 16.84$). Consequently, the increase/decrease of the Nusselt number shown in Table I when $\mathrm{Gr}_\tau \neq 0$ with respect to the value at $\mathrm{Gr}_\tau = 0$ can be attributed to the increase/decrease of the Reynolds number when Gr_τ is changed.

Figure 3(a) shows that the buoyancy-assisted effect on the H1 flow ($\mathrm{Gr} = +9000$) increased local wall heat fluxes in the stable wall, while the reduction of q_w produced by the buoyancy-opposed flow ($\mathrm{Gr} = -9000$) is more evident in the unstable wall. Figure 3(b) indicates an overall increase of the temperatures on the unstable and lateral walls and a decrease on the stable wall for the mixed convection H2 flows in comparison with the forced convection H2 flow.

B. Thermal energy budget

In the following discussion, for simplicity the nondimensional resolved average velocities, temperature, turbulent stresses, and turbulent heat fluxes are denoted as U_i, Θ, $\langle u_i' u_j' \rangle$, $\langle u_i' \theta' \rangle$, respectively. The mechanisms that affect the averaged thermal energy distribution of the resolved flow can be determined by examining the terms of its budget, which for a fully hydrodynamically and thermally developed flow can be written as

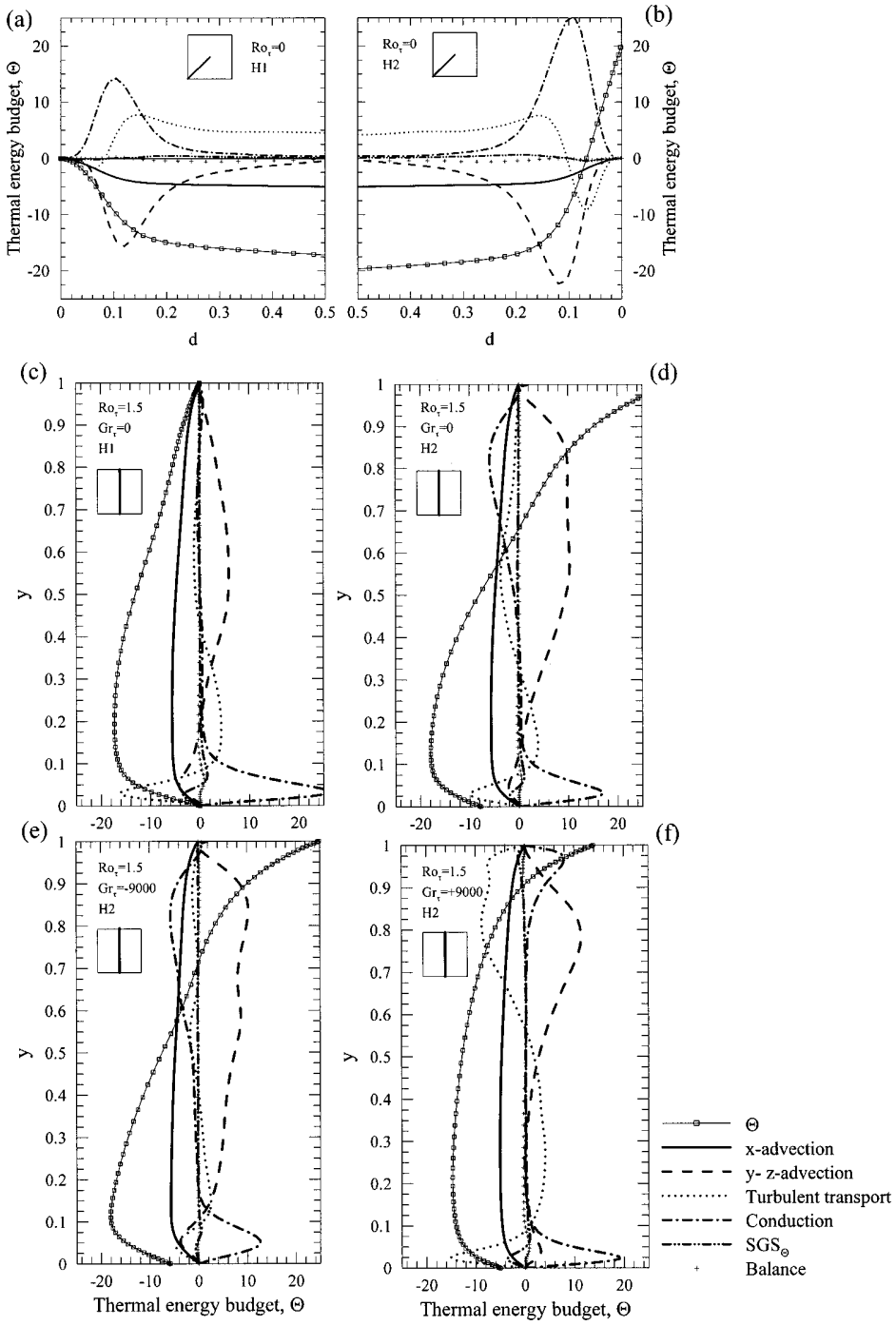

FIG. 4. Thermal energy budgets along (a) and (b) the corner bisector, $y=z$, and (c)–(f) horizontal walls bisector, $z=0.5$.

$$-4\frac{U}{U_b}-\left(V\frac{\partial\Theta}{\partial y}+W\frac{\partial\Theta}{\partial z}\right)-\left(\frac{\partial\langle v'\theta'\rangle}{\partial y}+\frac{\partial\langle w'\theta'\rangle}{\partial z}\right)+\frac{1}{\mathrm{Pr}\,\mathrm{Re}_\tau}\left(\frac{\partial^2}{\partial y^2}+\frac{\partial^2}{\partial z^2}\right)\Theta+\mathrm{SGS}_\Theta=0. \quad (6)$$

It can be seen that Eq. (6) is strongly linked to the momentum budget, which was analyzed by Pallares and Davidson[5] for isothermal rotating duct flow. The terms on the left-hand side of Eq. (6) are, from left to right, responsible for streamwise and cross-stream advection, turbulent transport, thermal conduction, and subgrid scale transport. Figure 4 shows the spatial distributions of the terms of the thermal energy budget as they appear in Eq. (6), and the corresponding temperature profiles.

It can be seen in Figs. 4(c)–4(f) that the maximum contribution of the SGS heat fluxes to the overall thermal budget was located near the unstable wall and that it represented about 20–25% of thermal conduction. This is consistent with the size of the SGS viscosity relative to molecular viscosity. For example, the maximum and the spatial average values of $\langle \nu_{\mathrm{SGS}}/\nu\rangle$ for the present LES of the nonrotating duct flow were 0.15 and 0.3. The corresponding values when the over-

all turbulent kinetic energy was enhanced by rotation (i.e., $\mathrm{Ro}_\tau = 1.5$, $\mathrm{Gr} = +9000$) increase to 0.18 and 0.4, respectively. The relatively small SGS stresses and heat fluxes in these simulations explains why the primary statistics of the flow depend little on the particular value of the constant SGS Prandtl number ($\mathrm{Pr}_{\mathrm{SGS}} = 0.4$) selected for the simulations.

Distributions of the terms in Eq. (6) along the wall bisectors for H1 and H2 nonrotating duct flows behaved in a similar way. There are considerable differences, however, when comparing the profiles of the thermal energy budget along the corner bisectors in Fig. 4(a) for the H1 flow and in Fig. 4(b) for the H2 flow. It can be seen that SGS transport contributed little to the overall averaged thermal budget. Streamwise and cross-stream advection act as a sink in Eq. (6), according to Fig. 2(a) in which secondary flows transport cold fluid from the central part of the duct towards the corners. Heat conduction contributes as a source in Eq. (6) because temperatures were higher at the wall than in the fluid and the negative temperature gradient decreased towards the center of the duct. Near the corner, turbulent transport and advection helped decrease the corner temperature. In the central part of the duct, turbulence acted as a transport term between hot fluid close to the corner and cold fluid in the center of the duct. In this region, turbulent transport decreased temperature gradients, and therefore, molecular heat conduction. Comparison of Figs. 4(a) and 4(b) indicates that all heat transport terms are increased in the H2 flow because of the uniform heat flux distribution imposed near the corner, which produces relatively large temperature differences in this region. Note that the H1 and H2 flows have been computed by imposing the same averaged heat flux at the duct periphery. As shown in Fig. 3(a) heat transfer rates in the H1 flow are increased away from the corners, where the main shear stress attains maximum values. This makes overall heat transfer efficiency higher than in the H2 flow.

Figure 4(c) shows how rotation affects the terms in Eq. (6) along the horizontal wall bisectors ($z = 0.5$) at $\mathrm{Gr}_\tau = 0$ for the H1 flow. As previously shown, rotation affected the flow in two main ways: it generated persistent secondary momentum transfer [see, e.g., Fig. 2(b)] and increase/decreased the main shear stress ($\partial U/\partial y$) on the unstable/stable sides. Turbulent transport was confined to near the bottom wall where the friction velocity was about 10% higher than in the nonrotating case. All mechanisms of heat transfer were present near the unstable wall [see Fig. 4(c)]. Heat conduction from the bottom wall was balanced with heat advection and turbulent and SGS transport. In the H1 flow, the dominant mechanisms were vertical and streamwise heat advection in the stable side where the Taylor–Proudman regime developed (i.e., $\partial U/\partial z \approx 0$ and $\partial \Theta/\partial z \approx 0$). Thermal energy convected to this region by the secondary flow was convected along the streamwise direction by the axial velocity component. A similar situation occurred in the x-momentum budget in this region, where the imposed streamwise pressure gradient was balanced with the vertical convection.[5] These considerations allow rewriting the thermal energy and the x-momentum budgets in the central part of the duct for the H1 flow as

$$V\frac{d\Theta}{dy} \approx -\frac{4U}{U_b} \tag{7}$$

and

$$V\frac{dU}{dy} \approx 4, \tag{8}$$

respectively. According to Pallares and Davidson,[5] at $\mathrm{Ro}_\tau = 1.5$ the central part of the duct, where the Taylor–Proudman regime develops, is a region in which the total mean vorticity ($\omega_z = \mathrm{Ro}_\tau + dU/dy$) becomes approximately zero if the main shear stress vorticity (dU/dy) which is nearly constant is scaled with the averaged velocity in that region, U_0,

$$\frac{1}{U_0}\frac{dU}{dy} + \mathrm{Ro}_\tau \approx 0. \tag{9}$$

Equations (7)–(9) can be used to estimate the magnitude of the vertical velocity component and the vertical temperature gradient in the central part of the duct for the H1 flow by assuming $U_0 \approx U_b \approx U$ (i.e., $V \approx -4/\mathrm{Ro}_\tau U_b$ and $d\Theta/dy \approx U\,\mathrm{Ro}_\tau$). The simplified budgets in Eqs. (7) and (8) show that the vertical temperature gradient is of the same order of magnitude as the vertical U velocity gradient and the Prandtl number relating the vertical momentum and heat transfer ($\mathrm{Pr}_v = (dU/dy)/(d\Theta/dy)$) is of order 1.

Figure 4(d), corresponding to a H2 flow at $\mathrm{Gr}_\tau = 0$, shows that turbulent transport of thermal energy contributed significantly to the heat transfer between the fluid near the top hot wall and the central part of the duct. Each contribution by the vertical and horizontal components of the turbulent transport represents about 20% of the vertical heat convection in the budget in Fig. 4(d). Because of the relatively large temperature gradient between the top wall and the center of the duct, vertical advection, and thermal conduction on the stable side were considerably higher in the H2 flow than in the H1 flow. Comparison of Figs. 4(c) (H1 flow) and 4(d) (H2 flow) on the unstable side shows a reduction of the turbulence transport and vertical convection in the H2 flow according to the uniform distribution of wall heat flux imposed by the H2 boundary condition.

Figures 4(e) ($\mathrm{Gr}_\tau = -9000$) and 4(f) ($\mathrm{Gr}_\tau = 9000$) show how the Grashof number affected thermal energy budget for the H2 flow along the horizontal walls bisector ($z = 0.5$). It can be seen in Figs. 4(d) and 4(e) that reducing Gr_τ from 0 to -9000 slightly increases the turbulent transport and decreases the wall temperatures on the stable side [see Fig. 3(b)], where $\Theta > 0$ and the flow is buoyancy assisted. Correspondingly, the turbulent transport is reduced in the central part of the duct and in the unstable side, where $\Theta < 0$, i.e., the flow is buoyancy opposed. The effect of increasing the Grashof number from 0 to 9000 can be observed comparing Figs. 4(d) and 4(f). At $\mathrm{Gr}_\tau = +9000$ turbulent transport increases all the way along the duct cross section, especially on the stable side where the fluid and wall temperatures are decreased. This reduces the buoyancy-opposing effect of the centrifugal force. In the central part of the duct, cross-stream advection is reduced because of the intensification of turbulence transport, which considerably decreases the vertical temperature gradient.

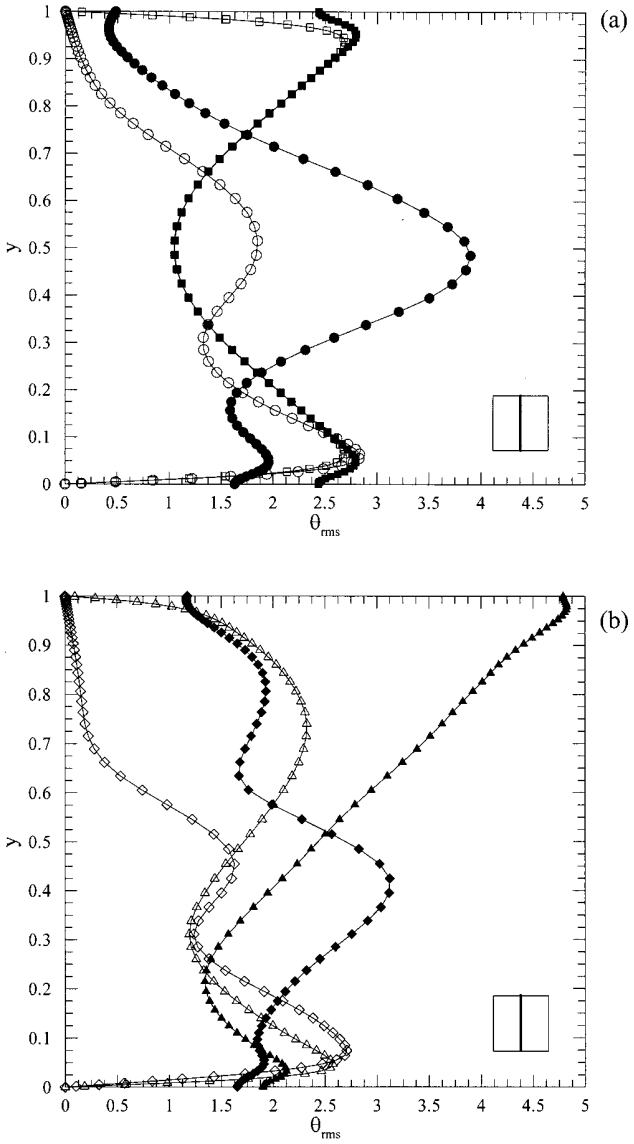

FIG. 5. Temperature fluctuation intensities along the horizontal walls bisector, z=0.5. Open and filled symbols correspond to H1 and H2 flows, respectively. (a) Forced convection flows ($Gr_\tau=0$); squares, $Ro_\tau=0$; circles $Ro_\tau=1.5$ and (b) mixed convection flows; triangles, $Ro_\tau=1.5$ and $Gr_\tau=+9000$; diamonds $Ro_\tau=1.5$ and $Gr_\tau=-9000$.

C. Temperature fluctuation intensities

Temperature fluctuation intensities along the horizontal walls bisector are shown in Figs. 5(a) and 5(b) which correspond to flows at $Gr_\tau=0$ and $Gr_\tau\neq0$, respectively.

It can be seen in Fig. 5(a) ($Gr_\tau=0$) that both the H1 and H2 boundary conditions produce the same temperature fluctuations in the central part of the duct for the nonrotating case ($Ro_\tau=0$). However, there are considerable differences at distances of about 0.1 D from the wall because the H2 boundary condition allows nonzero temperature fluctuations at the walls. The location and value of the maximum temperature fluctuations scaled with the local friction temperature at the wall bisector for the H1 flow are $y^+\approx19$ and $\mathrm{Max}(\theta_{rms})\approx2.6$, respectively. This agrees with channel flow DNS by Kasagi *et al.*,[11] who reported $y^+\approx18$ and $\mathrm{Max}(\theta_{rms})\approx2.4$. Correspondingly, for the H2 flow the location and the value of absolute maximum temperature fluctuations are $y^+\approx15$ and $\mathrm{Max}(\theta_{rms})\approx2.7$, respectively. A local maximum of temperature fluctuation is located at the wall with a value, scaled with the local friction temperature, of $(\theta_{rms})_w\approx2.3$. These results agree with DNS of channel flow with the H2 boundary condition carried out by Lu and Hetsroni,[12] who reported $y^+\approx18$, $\mathrm{Max}(\theta_{rms})\approx2.7$, and $(\theta_{rms})_w\approx2.2$. It can be seen that, despite the low grid resolution used in this region, the present LES correctly predicts the main characteristics of temperature fluctuation intensities.

Considerations about the spatial distributions of the Reynolds stresses in rotating channels and ducts can be deduced by analyzing the production terms of the turbulent stresses transport equations.[1,2,5] The production terms of the temperature intensity fluctuations, $P(\theta'^2)$, can be written for fully developed flow as

$$P(\theta'^2)=-\frac{4\langle u'\theta'\rangle}{U_b}-\langle v'\theta'\rangle\frac{\partial\Theta}{\partial y}-\langle w'\theta'\rangle\frac{\partial\Theta}{\partial z}. \qquad (10)$$

Computations of the averaged resolved terms of Eq. (10) for the present flow conditions have shown that the second and third terms dominate the production rate over most of the duct cross section. The first term only attains significant values where minimum temperatures occur ($\partial\Theta/\partial y=\partial\Theta/\partial z\approx0$).

As shown in Fig. 5(a), rotation decreases temperature fluctuations near the stable wall ($y=1$) because of the suppression of the turbulent heat fluxes [Fig. 4(c)]. It can be seen that the fluctuation profile of the H2 flow has a marked maximum in the center of the duct, where the term $\partial\Theta/\partial y$ and the vertical turbulent heat flux attains high values [see, e.g., Fig. 4(d)]. On the unstable side, near the bottom wall ($y=0$), the temperature fluctuation intensities of the rotating H2 flows are lower than the corresponding rotating H1 flows [Figs. 5(a) and 5(b)]. This agrees with the fact that on the unstable wall and near the wall bisector, the H1 boundary condition allows higher local heat fluxes [see Fig. 3(a)] than the H2 boundary condition. The positions of local minimum of $\langle\theta'^2\rangle$ near the unstable wall [Fig. 5(a), $Ro_\tau=1.5$] correspond to the positions of absolute minimum temperatures ($\partial\Theta/\partial y=0$) in the profiles in Figs. 4(c) and 4(d).

Figure 5(b), which corresponds to $Gr_\tau\neq0$, shows that at $Gr_\tau=-9000$ temperature fluctuations in the H1 flow are suppressed near the stable wall, while in the H2 flow they are enhanced in this region. This is shown in Fig. 4(e) by the increase in the turbulence transport of heat. Positive Grashof numbers affect temperature fluctuation intensities considerably [compare Figs. 5(a) and 5(b)]. Maximum temperature fluctuations in the central part of the duct at $Gr_\tau=0$ are displaced towards the stable wall ($y=1$) at $Gr_\tau=9000$, which agrees with the reactivation of the turbulence transport on the stable wall. It can be seen in Fig. 5(b), that, especially in the H2 flow, temperature fluctuations are high in this region.

D. Instantaneous flow visualizations

To show the origin of the above temperature fluctuation intensities and to illustrate the instantaneous flow structures generated, Fig. 6 shows three instantaneous states of the H2 flow. It should be noted that the instantaneous fields of Fig. 6 only serve as examples of the state of the flow at the different conditions considered.

Figures 6(a), 6(b), and 6(c) correspond to planes $x=3.8$ [Fig. 6(a), $\mathrm{Ro}_\tau=0$], $x=2.0$ [Fig. 6(b), $\mathrm{Ro}_\tau=1.5$, $\mathrm{Gr}_\tau=0$], and $x=4.0$ [Fig. 6(c), $\mathrm{Ro}_\tau=1.5$, $\mathrm{Gr}_\tau=9000$). In these figures, line and filled contours, which indicate constant values of the instantaneous x-velocity component fluctuations (u') and temperature fluctuations (θ'), respectively, are superimposed to the instantaneous cross-stream vector fields (v and w).

Figures 6(d1) ($\mathrm{Ro}_\tau=1.5$, $\mathrm{Gr}_\tau=0$), 6(e1) ($\mathrm{Ro}_\tau=1.5$, $\mathrm{Gr}_\tau=9000$), and 6(f1) ($\mathrm{Ro}_\tau=1.5$, $\mathrm{Gr}_\tau=9000$) show the flow structures in planes $0.4\leqslant y\leqslant 0.6$, $0\leqslant y\leqslant 0.2$, and $0.9\leqslant y\leqslant 1$, respectively, for the same instantaneous flow fields shown in Figs. 6(a) and 6(c). The flow structure are depicted in these figures using the definition of vortex core proposed by Jeong *et al.*[24] According to this definition the local pressure minima generated by the core of a vortex motion can be identified with negative values of λ_2, the second largest eigenvalue of the velocity gradient tensor. This definition has been used to detect and analyze quasistreamwise structures in isothermal channel flow,[24] isothermal rotating duct flow.[5] The isosurfaces of Figs. 6(d1), 6(e1), and 6(f1) have been colored dark or light gray depending on the sign of the instantaneous streamwise vorticity (ω_x') to illustrate the sense of rotation of the quasistreamwise structures. Dark gray surfaces correspond to $\omega_x'<0$ and light gray surfaces to $\omega_x'>0$.

The corresponding fluctuating vector fields and contours of temperature fluctuations to Figs. 6(d1), 6(e1), and 6(f1) are plotted in Figs. 6(d2) (plane $y=0.5$), 6(e2) (plane $y=0.1$), and 6(f2) (plane $y=0.9$).

Figure 6(a) ($Ro_\tau=0$) shows, near the walls, ejections of low momentum fluid alternated with sweeps of accelerated flow. This alternation is uniformly distributed along the duct periphery. There is a noticeable correspondence between regions of accelerated/decelerated flow with regions of high/low instantaneous temperature [see Figs. 6(a) and 6(d2)]. This indicates a strong correlation between the two fluctuations and therefore negative values of $\langle u'\theta'\rangle$. Points I and II, in Figs. 6(a), 6(d1), and 6(d2), indicate different views of two ejections occurring near the walls $z=0$ and $z=1$. Each ejection generates a pair of counter-rotating vortices that convect hot low momentum fluid form the wall towards the central part of the duct and cold high momentum fluid towards the wall [see points I and II in Fig. 6(a)]. It can be seen that the center of the vortex cores, shown in Fig. 6(a) with white circles and Fig. 6(d1) in terms of λ_2 [see points I and II in Fig. 6(d1)], separates positive temperature fluctuations from negative temperature fluctuations. This agrees with the convective transport of thermal energy produced by the vortical flow motion near the wall (i.e., cold high x-momentum fluid towards the wall and hot low x-momentum fluid away from the wall). Figures 6(d1) and 6(d2) show that the flow structures and the corresponding temperature and velocity fluctuations are inclined towards the central part of the duct. It can be seen in Fig. 6(d2) that, as the ejections depart from the wall, the vortical motions generate negative temperature fluctuations and positive x-velocity fluctuations near the wall. This temperature fluctuations distribution produced by the vortical motion is consistent with recent results from Matsubara *et al.*,[25] who educed coherent structures and the corresponding temperature fluctuation fields in a forced convection H2 channel flow.

At $\mathrm{Ro}_\tau=1.5$ and $\mathrm{Gr}_\tau=0$ [Fig. 6(b)] sweeps and ejections are confined near the unstable side. It can be seen that in the lower half of the duct a region with high temperature, centered at $y=0.3$ and $z=0.4$, is located above a region of accelerated flow ($y=0.05$ and $z=0.5$) and surrounded by two symmetrically distributed ejections ($y=0.05$, $z=0.3$, and $y=0.05$, $z=0.7$). Several instantaneous flow fields have shown that this situation often occurs and that temperature fluctuations in the central part of the duct are produced when cross-stream flow field convects hot fluid from the stable side of the central part of the duct. Note that in the H2 flow, temperature is on average higher along the horizontal wall bisectors than near the side walls [Fig. 2(b1)]. In fact, spatial distributions of the turbulent heat fluxes (not shown) show that in the central part of the duct both $\langle v'\theta'\rangle$ and $\langle w'\theta'\rangle$ attain significant values, which agrees with the position of the marked maximum of temperature fluctuation intensities in the central part of the duct [Fig. 5(a)].

Figure 6(c) and Figs. 6(e1)–6(f2) show an instantaneous H2 flow field at $\mathrm{Gr}_\tau=+9000$. Comparison of Figs. 4(d), 6(b) ($\mathrm{Gr}_\tau=0$) and 4(f), 6(c) ($\mathrm{G}_\tau=+9000$) indicates that the increase in the main turbulent heat flux, $\langle u'\theta'\rangle$, specially near the stable wall ($y=1$), agrees with the increase in the overall turbulence level of the flow produced by the buoyancy-assisted effect. It can be seen comparing Figs. 6(b) and 6(c) that turbulence activity is similar near the unstable wall ($y=0$). This is also shown in Figs. 4(d) ($\mathrm{Gr}_\tau=0$) and 4(f) ($\mathrm{Gr}_\tau=+9000$), where the turbulence transport terms contribute in a similar way near $y=0$ in both cases. Figures 6(c) (plane $x=4$) and 6(e2) (plane $y=0.1$) show that a persistent ejection occurs along the x direction near the unstable wall bisector (see point III). Near the stable wall ($y=1$), the buoyancy-assisted effect generates considerable mixing, as can be inferred comparing Figs. 6(b) and 6(c) and Figs. 4(d) and 4(f). The impingement on the stable wall ($y=1$) of the Coriolis-driven secondary flows, which occurs near the sidewalls $z=0$ and $z=1$, produces a row of quasistreamwise vortices near the top edges of the duct ($y=1$, $z=0$ and $y=1$, $z=1$) [see Fig. 6(f1)]. Accordingly, in Fig. 6(f1), flow structures with negative/positive streamwise vorticity predominate near $z=0/z=1$. Near the stable wall bisector ($y=1$, $z=0.5$), sweeps, marked with points IV to VII in Fig. 6(f2), generate pairs of counter-rotating vortices [see points IV to VII in Fig. 6(f1)]. Comparison of Figs. 6(f1) and 6(e1) shows that near the stable wall there is a high density of elongated instantaneous flow structures, while structures near the unstable wall are shorter and more dispersed. The noticeable turbulent activity near the stable wall at $\mathrm{Gr}_\tau=+9000$ [see

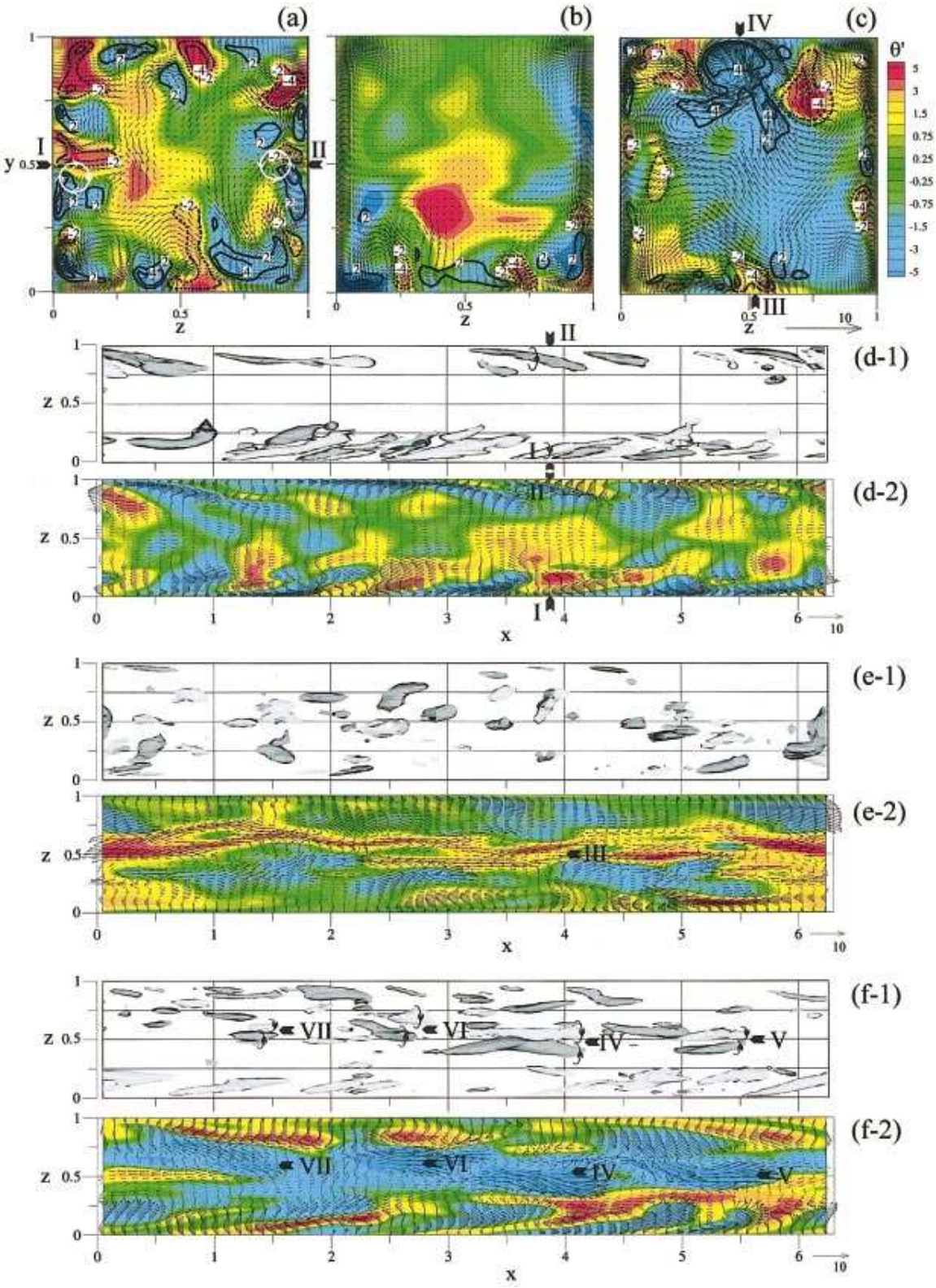

FIG. 6. (Color) 2D views of instantaneous H2 flows. (a), (b), and (c) Vertical cross sections. Line contours of streamwise velocity component fluctuations (u'), filled contours of temperature fluctuations (θ') and cross-stream vector field (v,w). (a) $\mathrm{Ro}_\tau=0$, plane $x=3.8$; (b) $\mathrm{Ro}_\tau=1.5$, $\mathrm{Gr}_\tau=0$, plane $x=2$, and (c) $\mathrm{Ro}_\tau=1.5$, $\mathrm{Gr}_\tau=+9000$, plane $x=4$. (d), (e), and (f) Horizontal planes (d1), (e1), and (f1). Instantaneous flow structures in terms of the isosurface $\lambda_2=-500$ in planes $0.4\leqslant y\leqslant 0.6$ [(d1) $\mathrm{Ro}_\tau=0$], $0\leqslant y\leqslant 0.2$ [(e1), $\mathrm{Ro}_\tau=1.5$, $\mathrm{Gr}_\tau=+9000$], and $0.9\leqslant y\leqslant 1$ [(f1), $\mathrm{Ro}_\tau=1.5$, $\mathrm{Gr}_\tau=+9000$]. (d2), (e2), and (f2). Temperature fluctuations (θ') and fluctuating vector field (u',v') in planes $y=0.5$ [(d2), $\mathrm{Ro}_\tau=0$], $y=0.1$ [(e2), $\mathrm{Ro}_\tau=1.5$, $\mathrm{Gr}_\tau=+9000$], and $y=0.9$ [(f1), $\mathrm{Ro}_\tau=1.5$, $\mathrm{Gr}_\tau=+9000$].

Figs. 6(a), 6(f1), and 6(f2)] agrees with the large temperature fluctuations intensities in Fig. 5(b) along the horizontal wall bisector.

IV. CONCLUSIONS

Fully developed turbulent forced and mixed convection flows at low Reynolds numbers in a rotating square duct has been simulated using a second order code with a one-equation dynamic subgrid scale model. Two boundary conditions for the energy equation were examined: constant peripheral wall temperature (H1) and uniform peripheral wall heat flux (H2). For the simulated nonrotating flows, the H1 boundary condition for temperature produced a higher overall heat transfer rate than the H2 boundary condition because of the presence of the corners. Analysis of the terms of the time-averaged thermal energy budget shows that the heat transfer processes in a rotating forced convection H1 flow are analogous to the *x*-momentum transfer processes. The variation of the wall temperature induced by rotation in the H2 flows produced larger temperature gradients within the fluid than the H1 flows. The H1 flow is therefore more efficient in transferring heat than the H2 flow since there are no significant differences in the overall Nusselt number of the H1 rotating forced flow and that of the H2 rotating force flow. The centrifugal buoyancy-assisted/-opposed effect increases/decreases the overall turbulence of the H1 and H2 flows, according to the changes induced by rotation in the streamwise turbulent heat flux.

ACKNOWLEDGMENT

J.P. was supported by the Department of Thermo and Fluid Dynamics of Chalmers University of Technology to carry out this study during his stay in the department.

[1] J. P. Johnston, R. M. Hallen, and D. K. Lezius, "Effects of spanwise rotation on the structure of two-dimensional fully developed turbulent channel flow," J. Fluid Mech. **56**, 533 (1972).
[2] R. Kristoffersen and H. Andersson, "Direct simulations of low-Reynolds-number turbulent flow in a rotating channel," J. Fluid Mech. **256**, 163 (1993).
[3] K. Alvelius, "Studies of turbulence and its modeling through large eddy- and direct numerical simulation," Ph.D. thesis, Department of Mechanics, Royal Institute of Technology, Stockholm, 1999.
[4] A. Murata and S. Mochizuki, "Effect of cross-sectional aspect ratio on turbulent heat transfer in an orthogonally rotating rectangular smooth duct," Int. J. Heat Mass Transf. **42**, 3803 (1999).
[5] J. Pallares and L. Davidson, "Large-eddy simulations of turbulent flow in a rotating square duct," Phys. Fluids **12**, 2878 (2000).
[6] M. Nishimura and N. Kasagi, "Direct numerical simulation of combined forced and natural turbulent convection in a rotating plane channel," in Proceedings of the 3rd KSME–JSME Thermal Engineering Conference, Kyongju, Korea, 1996, pp. III-77–III-82.
[7] J. J. Hwang, W. J. Wang, and C. K. Chen, "Buoyancy-driven flow reversal phenomena in radially rotating serpentine ducts," J. Heat Transfer **122**, 179 (2000).
[8] J. Kim and P. Moin, "Transport of passive scalars in a turbulent channel flow," *Turbulent Shear Flows VI* (Springer, Berlin, 1989).
[9] G. J. Hwang and T. C. Jen, "Convective heat transfer in rotating isothermal ducts," Int. J. Heat Mass Transf. **33**, 1817 (1990).
[10] S. L. Lyons, T. J. Hanratty, and J. B. McLaughlin, "Direct numerical simulation of passive heat transfer in a turbulent channel flow," Int. J. Heat Mass Transf. **34**, 1149 (1991).
[11] N. Kasagi, Y. Tomita, and A. Kuroda, "Direct numerical simulation of passive scalar field in a turbulent channel flow," J. Heat Transfer **114**, 598 (1992).
[12] D. M. Lu and G. Hetsroni, "Direct numerical simulation of a turbulent open channel flow with passive heat transfer," Int. J. Heat Mass Transf. **38**, 3241 (1995).
[13] G. Hetsroni, A. Mosyak, R. Rozenblit, and L. P. Yarin, "Thermal patterns on the smooth and rough walls in turbulent flows," Int. J. Heat Mass Transf. **42**, 3815 (1999).
[14] W. Kim and S. Menon, "Application of the localized dynamic subgrid-scale model to turbulent wall-bounded flows," AIAA Pap. 97-0210, 35th Aerospace Sciences Meeting and Exhibit, Reno, NV, 1997.
[15] R. K. Shah and M. S. Bhatti, "Laminar convective heat transfer in ducts," in *Handbook of Single-Phase Convective Heat Transfer*, edited by S. Kakac, R. K. Shah, and W. Aung (Wiley, New York, 1987).
[16] A. Sohankar and L. Davidson, "Effect of inclined vortex generators on heat transfer enhancement in a three-dimensional channel," Numer. Heat Transfer **39**, 433 (2001).
[17] L. Davidson, "Hybrid LES-RANS: A combination of a one-equation SGS model and a k-omega model for predicting recirculating flows," ECCOMAS CFD Conference, Swansea, UK, 2001.
[18] P. Emvin, "The full multigrid method applied to turbulent flow in ventilated enclosures using structured and unstructured grids," Ph.D. thesis, Department of Thermo and Fluid Dynamics, Chalmers University of Technology, Gothenburg, 1997.
[19] J. Pallares and L. Davidson, "Large-eddy simulations of turbulent flows in stationary and rotating channels and in a stationary square duct," Department of Thermo and Fluid Dynamics Report No. 00/3, Chalmers University of Technology, Gothenburg, 2000.
[20] G. E. Martensson, J. Gunnarsson, A. V. Johanson, and H. Moberg, "Experimental investigation of rapidly rotating turbulent duct flow," in Proceedings of the 2nd Turbulence and Shear Flow Phenomena, Stockholm, Sweden, 2001, pp. 37–42.
[21] S. Gavrilakis, "Numerical simulations of low-Reynolds-number turbulent flow through a straight square duct," J. Fluid Mech. **244**, 101 (1992).
[22] A. Huser and S. Biringen, "Direct numerical simulation of turbulent flow in a square duct," J. Fluid Mech. **257**, 65 (1993).
[23] V. Gnielinski, "New equations for heat and mass transfer in turbulent pipe and channel flow," Int. Chem. Eng. **16**, 359 (1976).
[24] J. Jeong, F. Hussain, W. Schoppa, and J. Kim, "Coherent structures near the wall in a turbulent channel flow," J. Fluid Mech. **332**, 185 (1997).
[25] K. Matsubara, M. Kobayashi, T. Sakai, and H. Suto, "A study on spanwise heat transfer in a turbulent channel flow—eduction of coherent structures by a conditional sampling technique," Int. J. Heat Fluid Flow **22**, 213 (2001).